



CRANFIELD UNIVERSITY

**A STUDENT**

**TITLE OF THE RESEARCH PROJECT  
IN CAPITALS**

SCHOOL OF ENGINEERING

MSc THESIS



CRANFIELD UNIVERSITY

SCHOOL OF ENGINEERING

MSc THESIS

Academic Year 2005-06

A STUDENT

Title of the research project

Supervisor: Dr Spock

August 2006

This thesis is submitted in partial (45%) fulfillment of the requirements for the degree of  
Master of Science

©Cranfield University 2006. All rights reserved. No part of this publication may be  
reproduced without the written permission of the copyright owner.



# Contents

Abstract . . . . .	i
Zusammenfassung . . . . .	i
Preamble . . . . .	i
Task assignement . . . . .	i
Declaration of Originality . . . . .	i
List of Figures . . . . .	iii
List of Tables . . . . .	v
Abbreviations . . . . .	vi
 <b>1 State-of-the-art</b>	 <b>1</b>
1.1 Morphing aircraft . . . . .	1
1.2 Wing twist morphing . . . . .	3
 <b>2 Wing Box model</b>	 <b>4</b>
2.1 Introduction . . . . .	4
2.2 Concept . . . . .	4
2.3 Analytical model . . . . .	4
2.4 Computational model . . . . .	6
2.4.1 Sub-parts and parametrization of the model . . . . .	6
2.4.2 Attachment points modeling . . . . .	11
 <b>3 Results</b>	 <b>14</b>
3.1 Introduction . . . . .	14

3.2	Parametric study on the analytical model . . . . .	14
3.2.1	Results . . . . .	14
3.2.2	Discussion of the results . . . . .	21
3.3	Parametric study on the computational model . . . . .	21
	Bibliography . . . . .	22

# List of Figures

1.1	Wright Brothers 1899 kite . . . . .	2
1.2	Shape morphing wing classification . . . . .	3
2.1	Schematic view of the beam closed section . . . . .	4
2.2	General assembly configuration for the computational model . . . . .	6
2.3	Overview of the chiral lattice part . . . . .	7
2.4	. . . . .	7
2.5	. . . . .	8
2.6	Overview of the wing-box in C-profile part . . . . .	9
2.7	Internal parameters of the wing-box C-profile part . . . . .	9
2.8	Overview of the tyre part . . . . .	10
2.9	Overview of the connection between tyre and lattice node . . . . .	10
2.10	Internal parameters of the tyre part . . . . .	11
2.11	First type of connection lattice-skin considered . . . . .	12
2.12	Second type of connection lattice-skin considered . . . . .	12
3.1	Influence of the cross-sectional aspect ratio $B/H$ on the torsional stiffness $GI_t$ . . . . .	15
3.2	Influence of the cross-sectional aspect ratio $B/H$ on the dimensionless shear centre position $y_{SC}/B$ . . . . .	15
3.3	Influence of the cross-sectional aspect ratio $B/H$ on the flexural stiffness $EI_y$ . . . . .	16
3.4	Influence of the cross-sectional aspect ratio $B/H$ on the deflection compliance . . . . .	16

---

3.5	Influence of the cross-sectional aspect ratio $B/H$ on the torsional compliance . . . . .	17
3.6	Influence of the wall thickness ratio $t_2/t_1$ on the torsional stiffness $GI_t$	17
3.7	Influence of the wall thickness ratio $t_2/t_1$ on the dimensionless shear centre position $y_{SC}/B$ . . . . .	18
3.8	Influence of the wall thickness ratio $t_2/t_1$ on the flexural stiffness $EI_y$	18
3.9	Influence of the thickness ratio $t_2/t_1$ on the deflection compliance . .	19
3.10	Influence of the thickness ratio $t_2/t_1$ on the torsional compliance . . .	19
3.11	Influence of the slenderness ratio $L/B$ on the deflection compliance .	20
3.12	Influence of the slenderness ratio $L/B$ on the torsional compliance . .	20



# List of Tables

2.1	Parameters used for the lattice model . . . . .	8
-----	---	---

# List of symbols

$A$	Cross sectional area	$[\text{mm}^2]$
$B$	Width of the cross section	$[\text{mm}]$
$B_{\text{chiral}}$	Node depth	$[\text{mm}]$
$E, E_1, E_2$	Young's modulus	$[\text{N}/\text{mm}^2]$
$e_{\text{chiral}}$	Dimensionless eccentricity	
$G, G_1, G_2$	Shear modulus	$[\text{N}/\text{mm}^2]$
$H$	Height of the cross section	$[\text{mm}]$
$I_t$	Torsional constant	$[\text{mm}^4]$
$L$	Length of the beam	$[\text{mm}]$
$L_{\text{chiral}}$	Ligament half length	$[\text{mm}]$
$M$	Number of unit cells in transversal direction	
$N$	Number of unit cells in spanwise direction	
$q_0$	Constant shear flow	$[\text{N}/\text{mm}]$
$q_{\text{C}}$	Close section shear flow	$[\text{N}/\text{mm}]$
$q_{\parallel}$	Open section shear flow	$[\text{N}/\text{mm}]$
$Q_z$	Force in direction of $z$	$[\text{N}]$
$r_{\text{chiral}}$	Node radius	$[\text{mm}]$
$S_{E_y}$	First moment of area	$[\text{N mm}]$
$t, t_1, t_2$	Wall thickness	$[\text{mm}]$
$w, w_0$	Displacements in direction of $z$	$[\text{N}/\text{mm}^2]$
$x$	Coordinate in the spanwise direction	$[\text{mm}]$
$y_{\text{ana}}, z_{\text{comp}}$	Coordinate in the chordwise direction for the analytical and computations reference systems	$[\text{mm}]$

---

$z_{\text{ana}}, y_{\text{comp}}$	Coordinate in the transversal direction for the analytical and computations reference systems	[mm]
$\nu$	Poisson's ratio	
$\phi, \phi_{\text{tip}}$	Twist angle	[deg]
$\Phi_y$	Flexural stiffness	[N mm <sup>2</sup> ]

**Abbreviations**

ABS	Acrylonitrile butadiene styrene
CAE	Complete Abaqus Environment
CMAS	Composite Materials and Adaptive Structures Lab
FEM	Finite element method
NASA	National Aeronautics and Space Agency

# Chapter 1

## State-of-the-art

In the present chapter, a review of the current technology related to the topic of this work will be reviewed. Firstly, a review of the different morphing wing technologies will be introduced. Secondly, a particular focus on the state-of-the-art of technology exploit in the current project will be presented.

### 1.1 Morphing aircraft

The interest in morphing of the aerodynamic surfaces has accompany aerospace history since the beginning. Since the first heavier-than-air flight in 1903, when the Wright Brothers designed and build the first controlled, sustained flight of a powered heavier-than-air aircraft. Their concept of aircraft did not provide importance to built-in stability but absolute control of the aircraft by the pilot. For this reason, they deliberately designed their first aircraft with anhedral wing that make it be dynamically unstable to perturbations in sideslip but more maneuverable in the lateral direction. In order to achieve roll control, they decided to incorporate a mechanism that would allow the wings to twist by pulling from cables, as it can be seen in Figure 1.1. This was the first ever use of morphing of an aerodynamic surface for aircraft control. Since them, the necessity of enhanced performance and higher airspeed brought the requirement of stiffer wing structures to avoid aeroelastic instabilities. This caused the invention o

On conventional aircraft, the need to modify the airflow around the airfoil at different flight conditions is achieve through discrete hinged mechanics such as flaps and ailerons. This mechanism perform well in a limited range around the design point while the outside this range, they have a negative influence in the aerodynamics. The necessary discontinuities in the surface bring forward the boundary layer transition from laminar to turbulent regime. Being able to modify the airflow without discontinuities on the airfoil skin would come along with notable reduction in fuel consumption.

New interest has raised in the recent years in aircraft morphing, mainly due to the appearance of new smart materials that allow more efficient mechanical design that

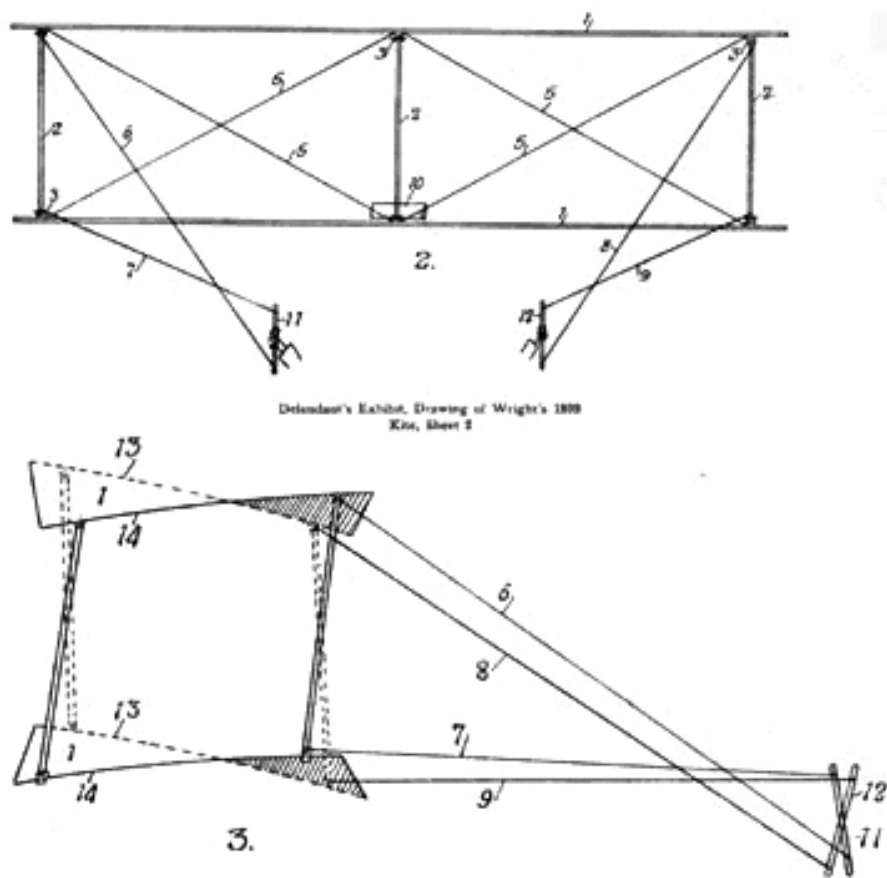


Figure 1.1: Wright 1899 kite: front and side views, with control sticks. Wing-warping is shown in lower view. [1]

do not necessarily incur weight increase [2]. Another reason that is pushing forward new aircraft morphing technologies is that missions today are in need of higher aircraft versatility to decrease operational costs in the commercial aviation field and aim smaller and more distributed targets in the military field. For example, Airbus has recently patented a design of a downwardly foldable wing tip device applicable for a large passenger aircraft [3].

A general classification of different wing morphing concepts can be seen in Figure 1.2: planform modification through variation of sweep angle, span or chord; out-of-plane alteration involving twist, dihedral angle and spanwise bending, and airfoil adjustment achieved by modifications of the airfoil chamber and/or thickness. Under this classification, the morphing technology that is the focus of this project is located under the out-of-plane branch and twist modification.

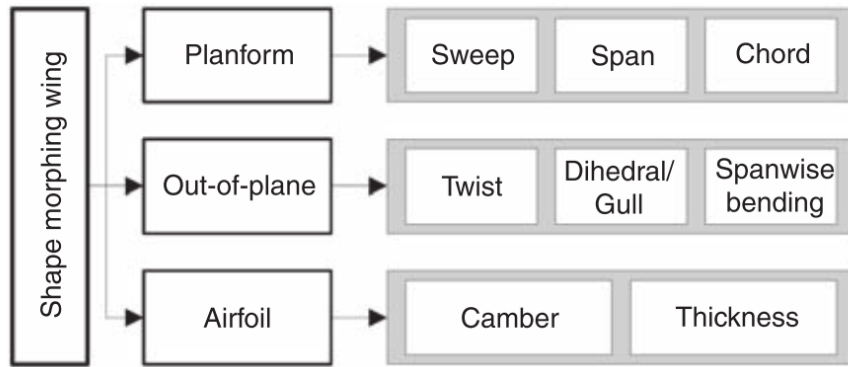


Figure 1.2: Shape morphing wing classification. [4]

Morphing designs may also benefit from geo-metrically flexible structures if the aeroelastic energy from the airstream can be used to activate the shape changing and tabs can maintain the shape using aero-elastic control.

## 1.2 Wing twist morphing

In the present section, an analysis of different concepts used to achieve .

The concept of varie the wing twist to modify the airfoil exploits the

## Chapter 2

# Wing Box model

### 2.1 Introduction

### 2.2 Concept

### 2.3 Analytical model

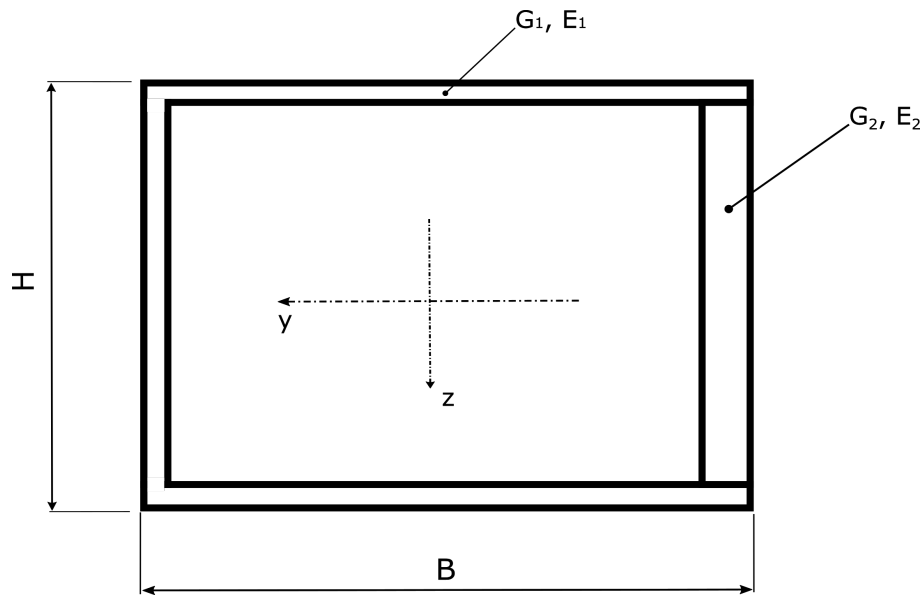


Figure 2.1: Schematic view of the beam closed section. The dimensions are given by the width  $B$  and the height  $H$ . For the upper, lower and left elements, the shear modulus and the elastic modulus are given by  $G_1$  and  $E_1$ , respectively. For the right element, the same mechanical properties are given by  $G_2$  and  $E_2$ .

$$GI_t = \frac{4A_0^2}{\oint \frac{ds}{G(s)t(s)}} \quad (2.1)$$

Furthermore, the shear flow distribution in the beam will be calculated. In other to consider this distribution, the profile can be considered to be cut at one point, resulting on a opened section. The shear flow  $q_{\parallel}(s)$  for this case can be calculated using Equation 2.2. The corresponding shear flow for a closed section can be obtained using the Equation 2.3.

$$q_{\parallel}(s) = -\frac{Q_z}{\Phi_y} S_{E_y}(s) \quad (2.2)$$

$$q_C(s) = q_{\parallel}(s) + q_0 \quad (2.3)$$

where  $Q_z$  is the force applied in the  $z$  direction and  $\Phi_y$  is the flexural stiffness given by Equation 2.4. Additionally,  $S_{E_y}$  is the so called static moment or first moment of area, which is calculated through the integral shown in Equation 2.5. Also, the variable  $q_0$  represents the shear flow at the boundary that results from the torsion of the beam and can be calculated using the Equation 2.6.

$$\Phi_y = \int \int E(y, z) z^2 dy dz \quad (2.4)$$

$$S_{E_y}(s) = \int_0^s E(s) t(s) z(s) ds \quad (2.5)$$

$$q_0 = \frac{Q_z \oint_s \frac{S_{E_y}(s)}{G(s)t(s)} ds}{\Phi_y \oint_s \frac{1}{G(s)t(s)} ds} \quad (2.6)$$

Now, the shear centre position in the beam transversal section will be calculated for the case of open section. Given that beam mechanical properties and geometrical dimensions are symmetric around  $y$  axis, the shear centre position in the  $z$  axis will be  $z_{SC} = 0$ . On the other hand, the shear centre position in the  $y$  axis will be given by the Equation 2.7.

$$y_{SC,open} = \frac{1}{Q_z} \oint_s q_C(s) r(s) ds \quad (2.7)$$

where  $r$  represents the perpendicular distance to the coordinate origin.

Now, it is necessary that equilibrium exists between the torsional moment due to the shift of the shear centre (caused during the opening of the profile) and the moment due to the torsional shear flow of the closed profile. This condition can be mathematically expressed through Equation 2.8.

$$\begin{aligned} M_t &= Q_z (y_{SC,open} - y_{SC,closed}) \\ &= 2A_0 q_0 \end{aligned} \quad (2.8)$$

Finally, the total shear flow  $q(s)$  results from the superposition of the shear flow of the open profile  $q_C$  and the constant shear flow due to torsion  $q_0$ , as shown in the Equation 2.9.

$$q(s) = q_C(s) - q_0 \quad (2.9)$$



## 2.4 Computational model

The computational model of the wing box was build using Abaqus CAE commercial software. It consisted on three main elements: the wing-box with C-profile, the lattice constituted of the chiral elements, a closed rib at the tip of the box and a closed rib at the root of the box. A general overview of the assembly of the different parts can be seen in Figure 2.2.

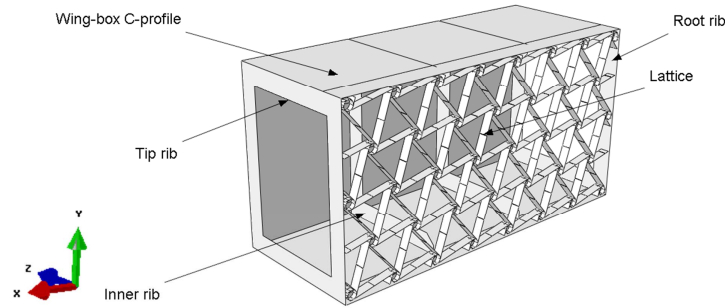


Figure 2.2: General assembly configuration for the computational model. The different parts for the general configuration include the wing-box profile, the lattice and the pair of ribs located at the tip and the root of the wing-box.

### 2.4.1 Sub-parts and parametrization of the model

#### Lattice of chiral elements

The model of the lattice structure is constituted of a series of interconnected lattices and nodes. An overview of the corresponding part can be seen in Figure 2.3. The parameters used to characterize the element are shown in Table 2.1.

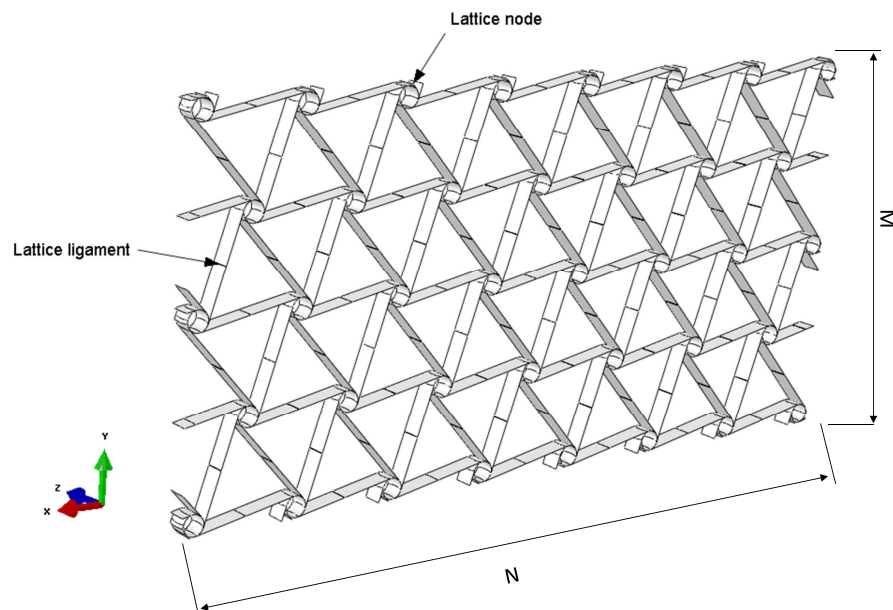


Figure 2.3: Overview of the chiral lattice part. The parameters  $M$  and  $N$  represent the number of unit cells

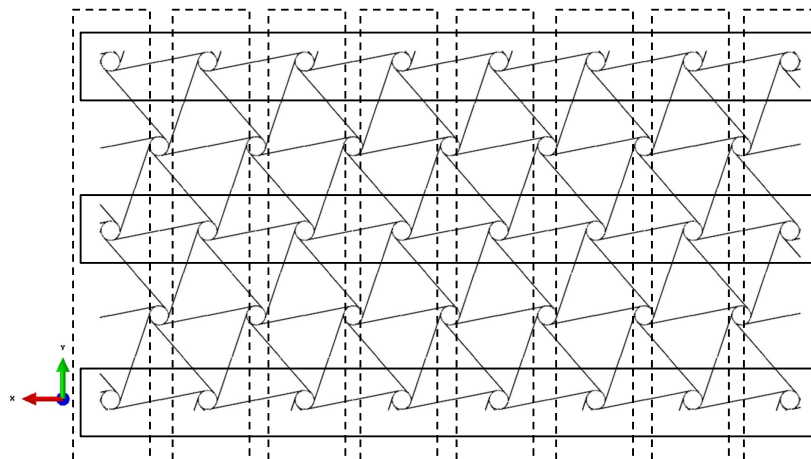


Figure 2.4:

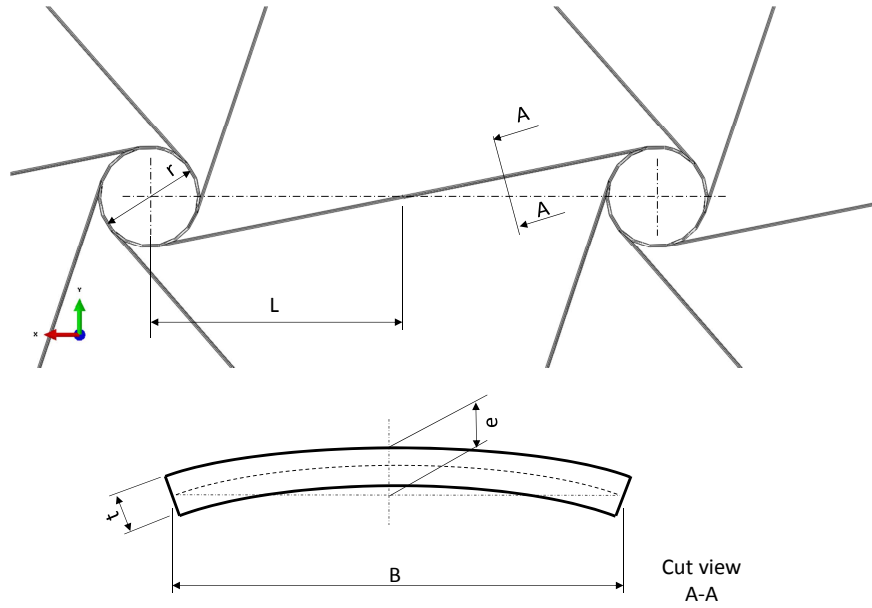


Figure 2.5:

Parameter	Symbol	Units	Nominal value
<b>Dimensions</b>			
Number of unit cells in spanwise direction	$N$		8
Number of unit cells in transversal direction	$M$		3
Dimensionless eccentricity ( $e/B$ )	$e_{\text{chiral}}$		0.01
Node radius	$r_{\text{chiral}}$	mm	10
Node depth	$B_{\text{chiral}}$	mm	20
Ligament half length	$L_{\text{chiral}}$	mm	50
<b>Material (ABS)</b>			
Young's modulus	$E_{\text{chiral}}$	N/mm <sup>2</sup>	31000
Poisson's ratio	$\nu_{\text{chiral}}$		0.3

Table 2.1: Parameters used for the lattice model. The mechanical properties of the material used correspond to ABS, which is a common thermoplastic polymer.

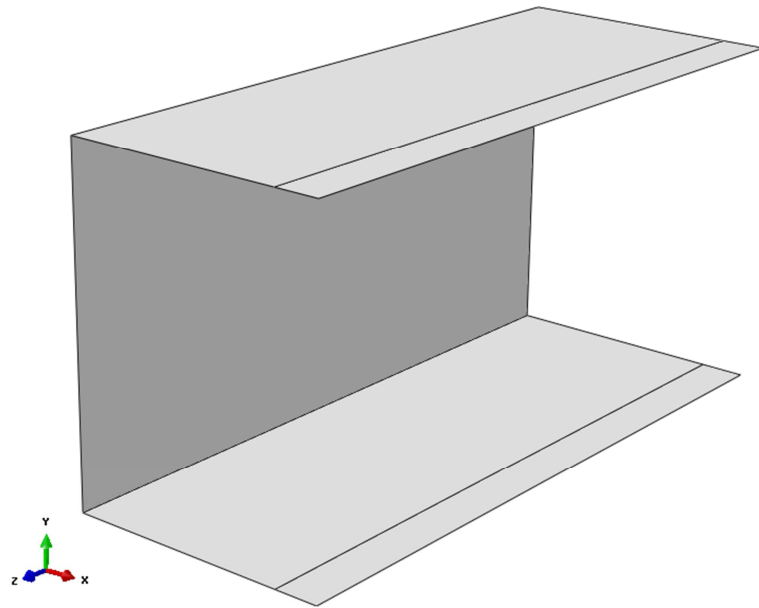


Figure 2.6: Overview of the wing-box in C-profile part

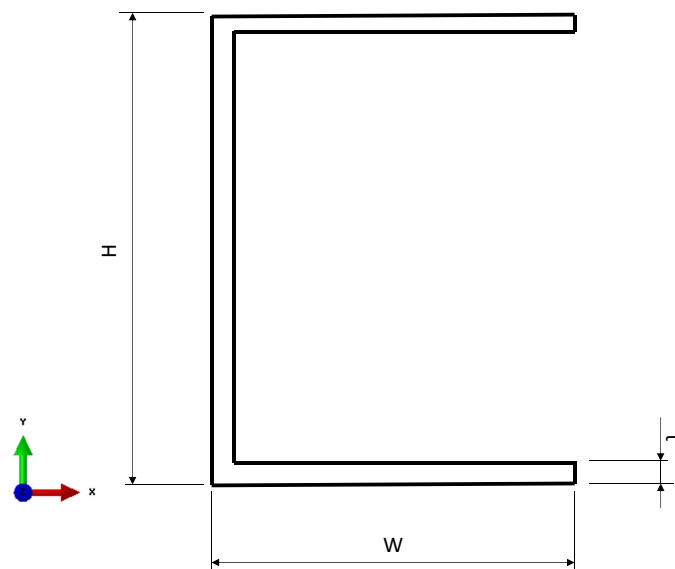


Figure 2.7: Internal parameters of the wing-box C-profile part

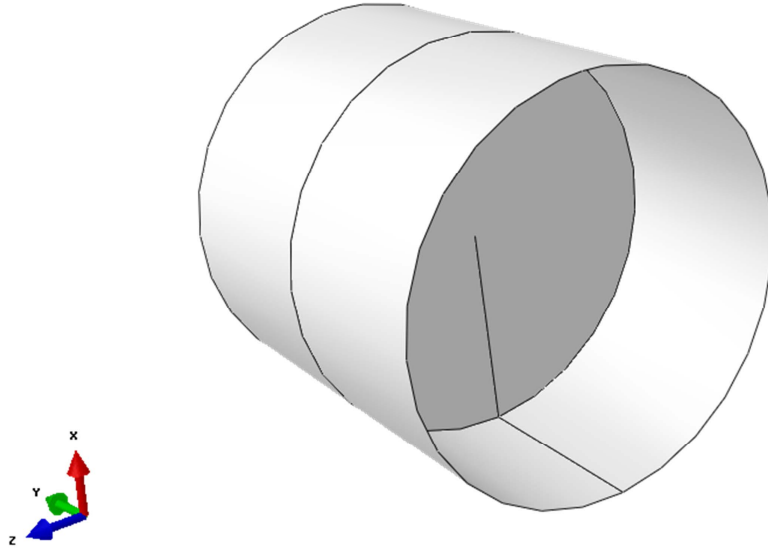


Figure 2.8: Overview of the tyre part.

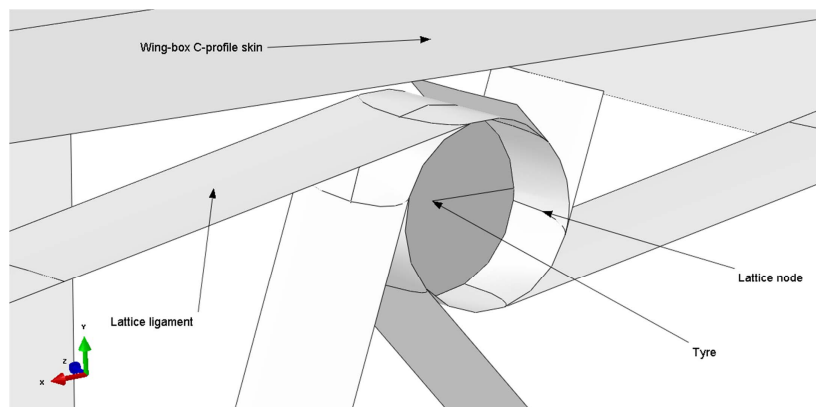


Figure 2.9: Overview of the connection between tyre and lattice node.

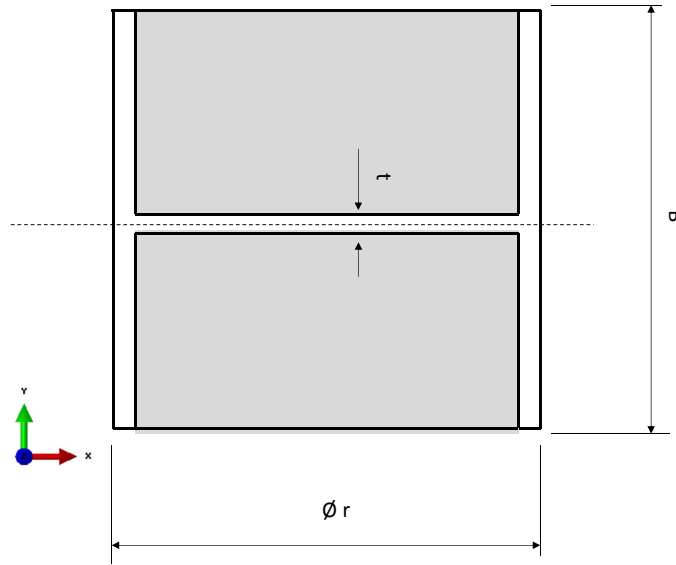


Figure 2.10: Internal parameters of the tyre part

## Wing-box in C-profile

### Ribs

### Lattice nodes

#### 2.4.2 Attachment points modeling

In the present subsection, the FEM modeling of the connection between the lattice nodes and the wing box is presented. The connection that will be modeled is the one that can be seen in Figure XX.

Two different connections will be modeled. Firstly, all the degrees of freedom of the lattice will be restricted except from the rotation around its own axis. An sketch showing this connection can be viewed in Figure 2.11. This was the design chosen for the manufactured demonstrator shown in Figure XX.

Another option for the modeling was to leave the lattice node displacement parallel to the skin unconstrained. This allows another degree of freedom for this element and therefore the connection between the node lattice and the skin is schematically like the one shown in Figure 2.12.

In order to model the connections shown in Figures 2.11 and 2.12, different different approaches were explored.

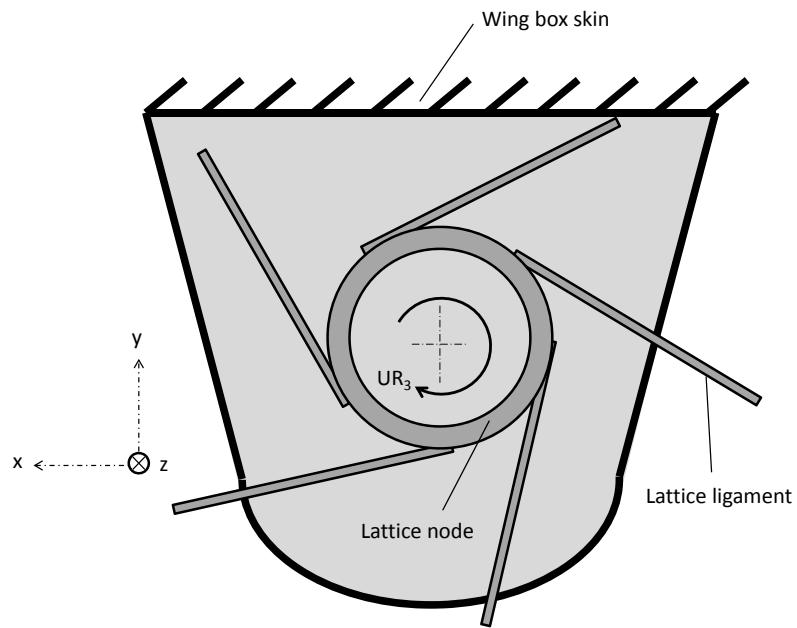


Figure 2.11: First type of connection lattice-skin considered.

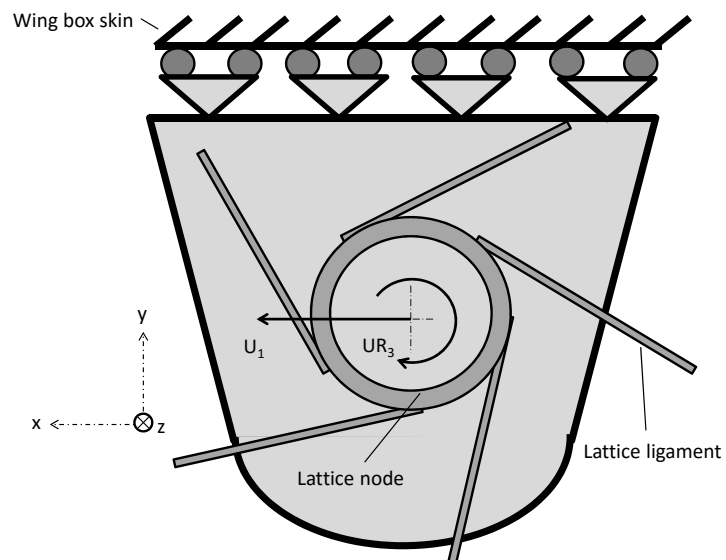


Figure 2.12: Second type of connection lattice-skin considered.





## Chapter 3

# Results

### 3.1 Introduction

### 3.2 Parametric study on the analytical model

In the present subsection, the variation of the beam properties for different parameter values will be shown. The beam geometry will be characterized through the cross-sectional aspect ratio  $B/H$ , the thickness ratio  $t_2/t_1$  and the slenderness ratio  $L/B$ . The effect of these parameters on the sectional properties, twist and bending stiffness, and flexural and twisting compliance will be shown. Additionally, the variance of the stiffness ratio  $E_1/E_2$  will also be included in the analysis.

#### 3.2.1 Results

The influence of the cross-sectional aspect ratio  $B/H$  on the torsional stiffness  $GI_t$ , the shear centre position  $y_{SC}$  and the flexural stiffness  $EI_y$  is shown in Figures 3.1, 3.2 and 3.3, respectively. On its side, the effect of thickness ratio  $t_2/t_1$  on the same three beam parameters is shown in Figures 3.6, 3.7 and 3.8.

Additionally, the effect of the cross-sectional aspect ratio  $B/H$  on the deflection and torsional compliance is shown on Figures 3.4 and 3.5, respectively. The corresponding plots when analysing the effect of the thickness ratio  $t_2/t_1$  on the deflection and torsional compliance are shown on Figures 3.9 and 3.10, respectively. The beam's torsional compliance will be expressed as fraction of the twist at the tip divided by the vertical force applied, that is  $|\phi_{tip}|/Q$ , while the beam deflection compliance will be expressed as fraction of the maximum vertical displacement at the tip divided by the vertical force applied, that is  $w_{0,tip}/Q$ .

The effect of the slenderness ratio  $L/B$  on the deflection and torsional compliances is shown in Figures 3.11 and 3.12, respectively.

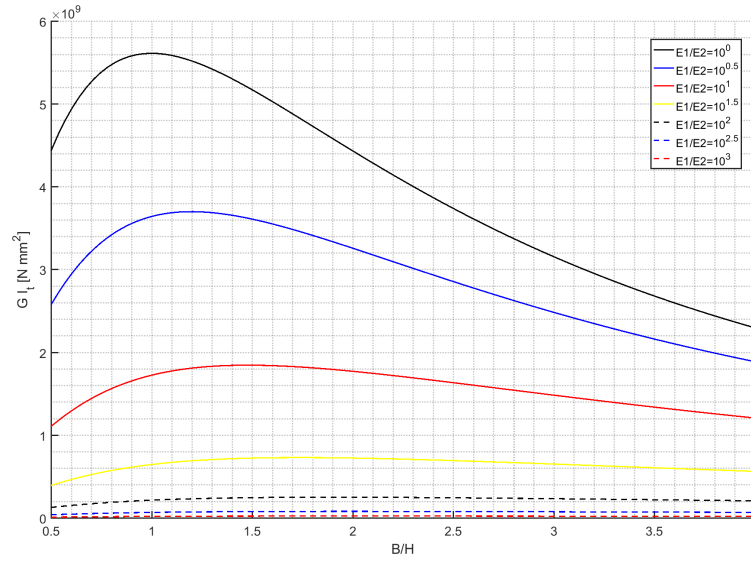


Figure 3.1: Influence of the cross-sectional aspect ratio  $B/H$  on the torsional stiffness  $GI_t$  is shown for various values of the stiffness ratio  $E_1/E_2$  ranging from  $10^0$  to  $10^3$ .

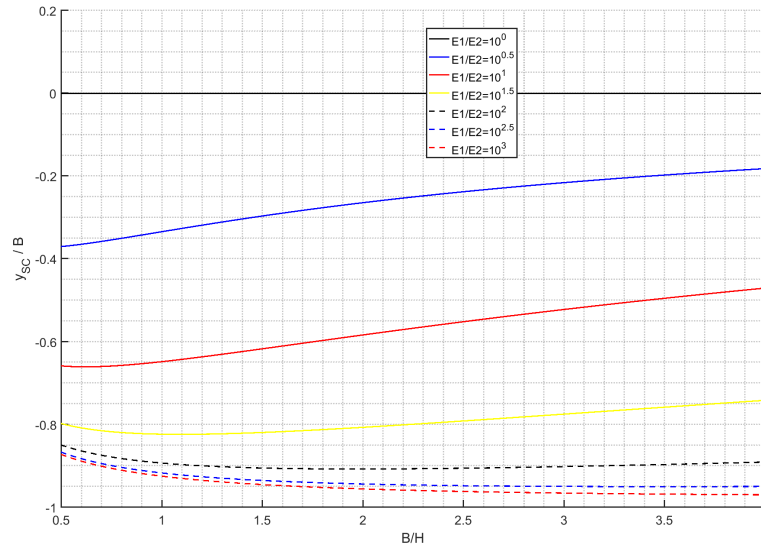


Figure 3.2: Influence of the cross-sectional aspect ratio  $B/H$  on the dimensionless shear centre position  $y_{SC}/B$  is shown for various values of the stiffness ratio  $E_1/E_2$  ranging from  $10^0$  to  $10^3$ .

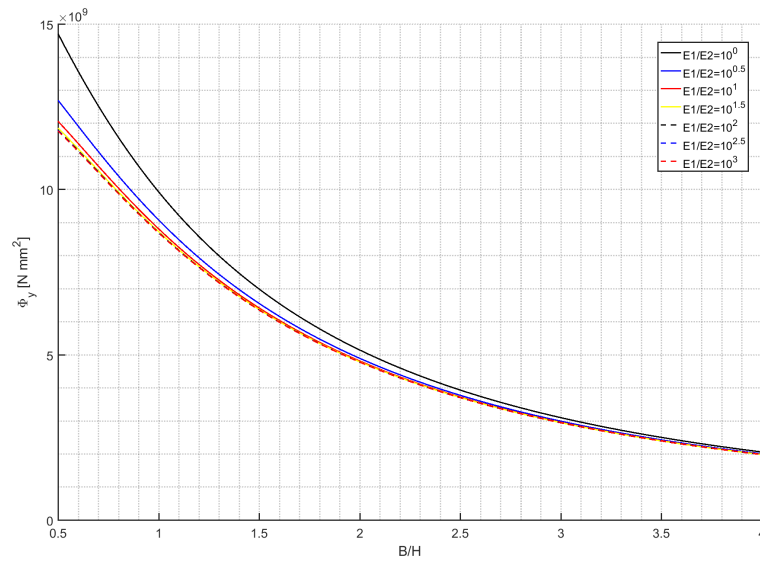


Figure 3.3: Influence of the cross-sectional aspect ratio  $B/H$  on the flexural stiffness  $EI_y = \Phi_y$  is shown for various values of the stiffness ratio  $E_1/E_2$  ranging from  $10^0$  to  $10^3$ .

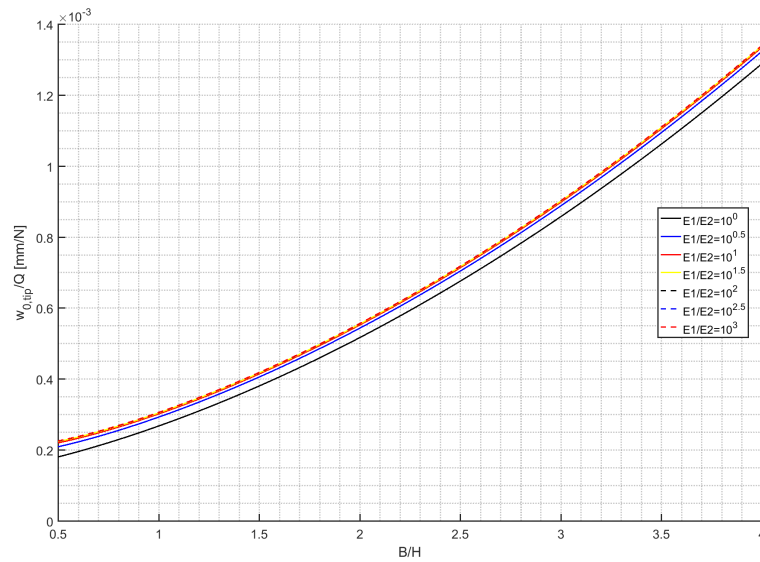


Figure 3.4: Influence of the cross-sectional aspect ratio  $B/H$  on the deflection compliance  $w_{0,\text{tip}}/Q$  is shown for various values of the stiffness ratio  $E_1/E_2$  ranging from  $10^0$  to  $10^3$ .

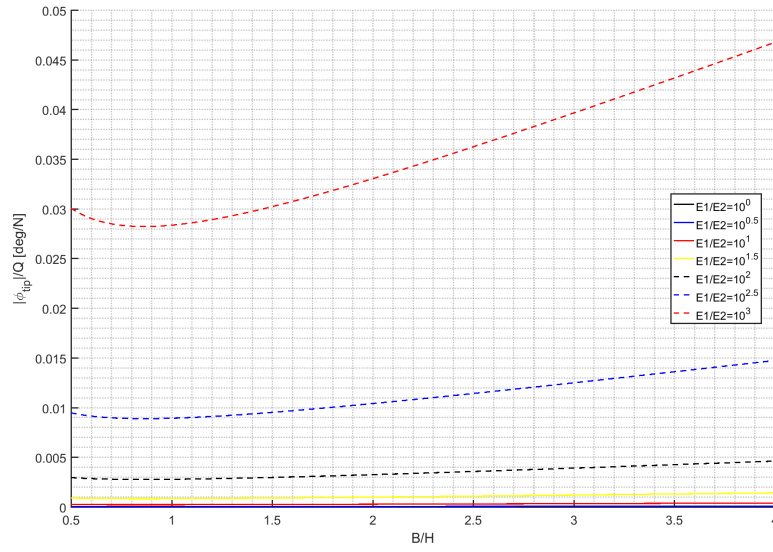


Figure 3.5: Influence of the cross-sectional aspect ratio  $B/H$  on the torsional compliance  $|\phi_{\text{tip}}|/Q$  is shown for various values of the stiffness ratio  $E_1/E_2$  ranging from  $10^0$  to  $10^3$ .

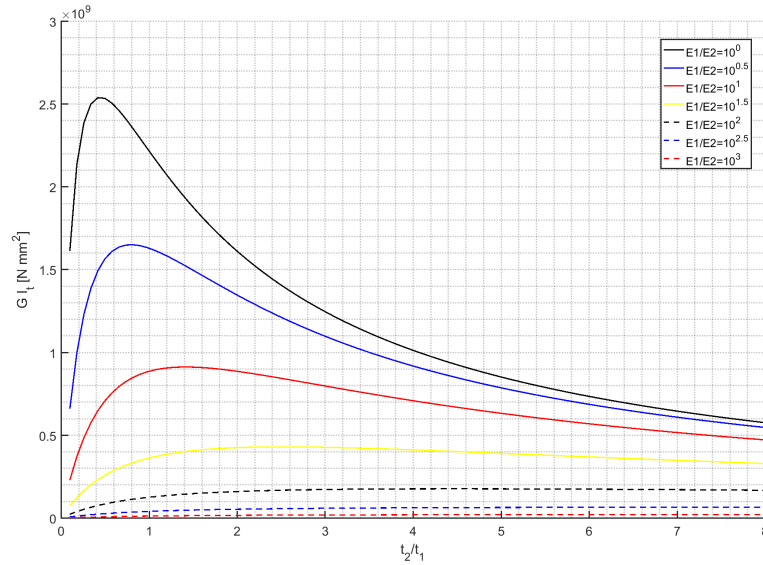


Figure 3.6: Influence of the wall thickness ratio  $t_2/t_1$  on the torsional stiffness  $GI_t$  shown for various values of the stiffness ratio  $E_1/E_2$  ranging from  $10^0$  to  $10^3$ .

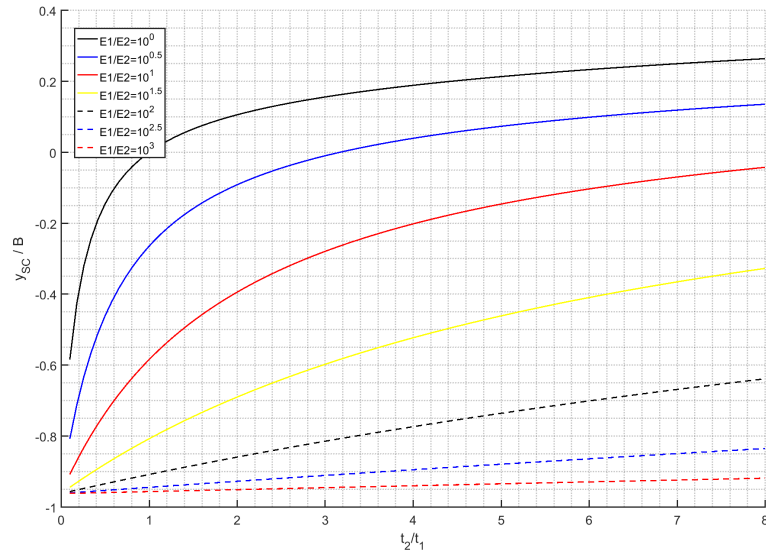


Figure 3.7: Influence of the wall thickness ratio  $t_2/t_1$  on the dimensionless shear centre position  $y_{SC}/B$  shown for various values of the stiffness ratio  $E_1/E_2$  ranging from  $10^0$  to  $10^3$ .

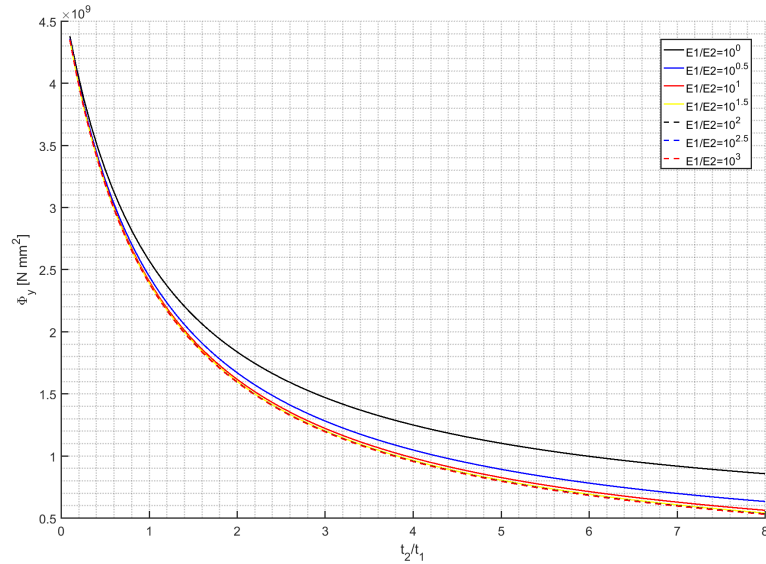


Figure 3.8: Influence of the wall thickness ratio  $t_2/t_1$  on the flexural stiffness  $EI_y = \Phi_y$  shown for various values of the stiffness ratio  $E_1/E_2$  ranging from  $10^0$  to  $10^3$ .

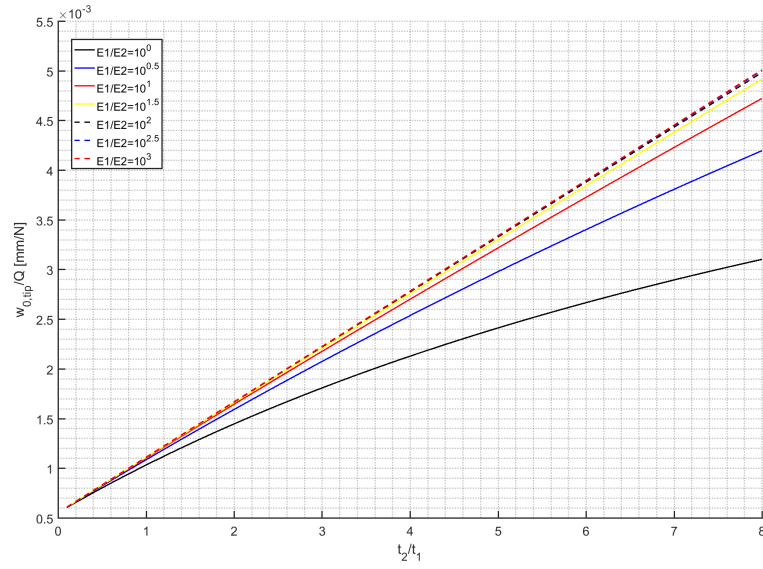


Figure 3.9: Influence of the thickness ratio  $t_2/t_1$  on the deflection compliance  $w_{0,\text{tip}}/Q$  is shown for various values of the stiffness ratio  $E_1/E_2$  ranging from  $10^0$  to  $10^3$ .

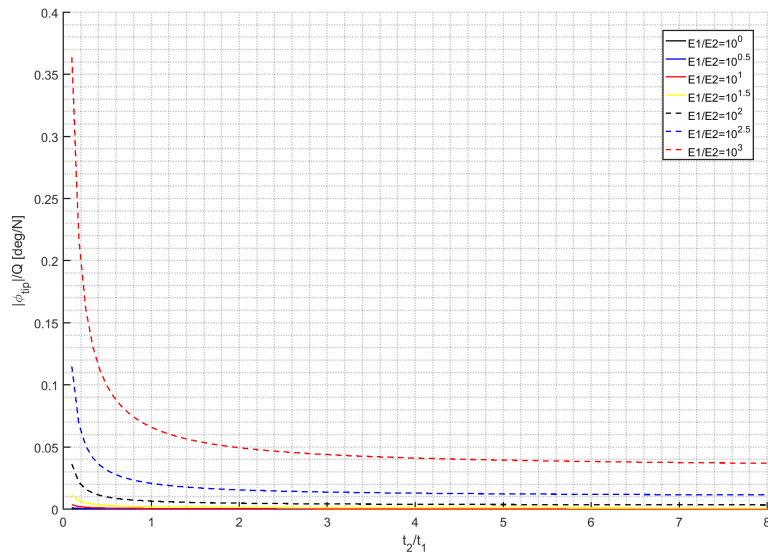


Figure 3.10: Influence of the thickness ratio  $t_2/t_1$  on the torsional compliance  $|\phi_{\text{tip}}|/Q$  is shown for various values of the stiffness ratio  $E_1/E_2$  ranging from  $10^0$  to  $10^3$ .

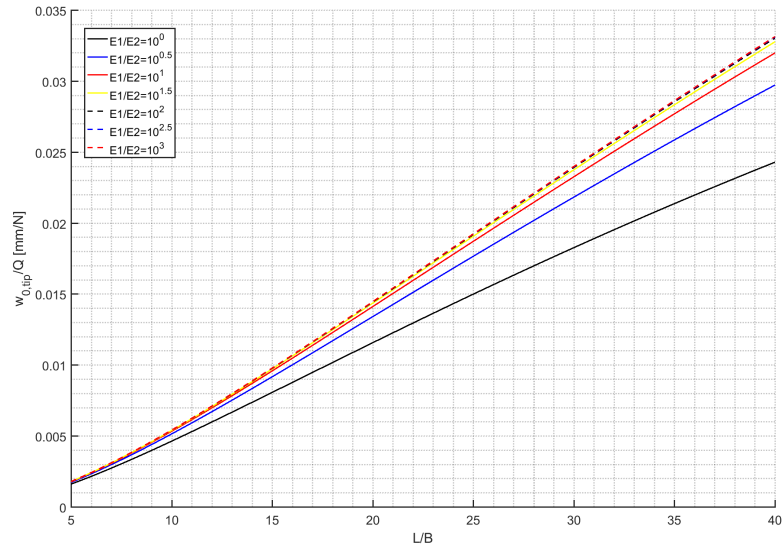


Figure 3.11: Influence of the slenderness ratio  $L/B$  on the deflection compliance  $w_{0,tip}/Q$  is shown for various values of the stiffness ratio  $E_1/E_2$  ranging from  $10^0$  to  $10^3$ .

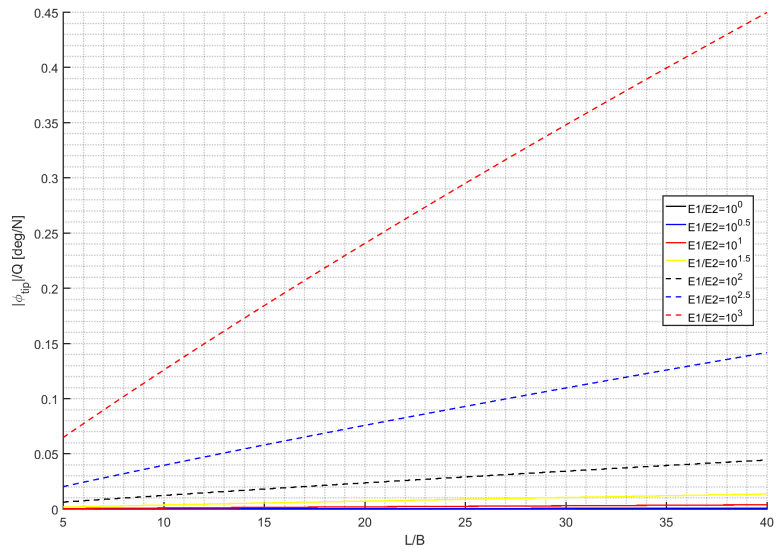


Figure 3.12: Influence of the slenderness ratio  $L/B$  on the torsional compliance  $|\phi_{tip}|/Q$  is shown for various values of the stiffness ratio  $E_1/E_2$  ranging from  $10^0$  to  $10^3$ .

### 3.2.2 Discussion of the results

The maximum torsional stiffness  $GI_t$  as a function on the cross-sectional aspect ratio  $B/H$  can be visualized in Figure 3.1. It can be seen that it appears for  $B/H = 1$  when  $E_1/E_2 = 1$ . Therefore, as it is also shown in [5], the closer the torsional stiffness to the doubly symmetric case, the higher its torsional stiffness. However, when  $E_1/E_2 > 10$ , the maximum torsional stiffness is shown to appear for  $B/H > 1$ . A similar conclusion can be extract when analysing the Figure 3.6, that shows the influence of the thickness ratio  $t_2/t_1$  on the torsional stiffness  $GI_t$ .

In Figure 3.2 it can be seen that for values  $E_2 \ll E_1$ , the shear centre position  $y_{SC}$  is approximately constant for  $B/H$  variations. In this context, the beam approximates its behavior as if it has an open profile section. However, as the value of  $E_1/E_2$  decreases, the influence of the ratio  $B/H$  increases showing a bigger influence of the web where the Young's modulus  $E_2$  applies. On the other hand, Figure 3.7 shows that the bigger the thickness ratio  $t_2/t_1$  is, the closer that the shear centre  $y_{SC}$  will be to the vertical axis of simmetry. However, for  $E_2 \ll E_1$  the influence of the thickness ratio  $t_2/t_1$  is reduced.

The influence of the cross-sectional aspect ratio  $B/H$  and the tickness ratio  $t_2/t_1$  on the flexural stiffness  $EI_y$  is shown to be bigger that that of the Young's modulus ratio  $E_1/E_2$ , as shown on Figures 3.3 and 3.8, respectively.

## 3.3 Parametric study on the computational model



# References

- [1] “Part of ”the dream of flight” online exhibit in the American Treasures section at the U.S. Library of Congress..” <http://www.loc.gov/exhibits/treasures/images/>. Accessed: 2017-07-29.
- [2] P. a. Lloyd, “Requirements for smart materials,” *Proceedings of the Institution of Mechanical Engineers, Part G: Journal of Aerospace Engineering*, vol. 221, no. 4, pp. 417–478, 2007.
- [3] S. Boye, “A passenger aircraft with a downwardly foldable wing tip device,” 2015.
- [4] S. Barbarino, O. Bilgen, R. M. Ajaj, M. I. Friswell, and D. J. Inman, “A Review of Morphing Aircraft,” *Journal of Intelligent Material Systems and Structures*, vol. 22, no. 9, pp. 823–877, 2011.
- [5] W. Raither, A. Bergamini, and P. Ermanni, “Profile beams with adaptive bending-twist coupling by adjustable shear centre location,” *Journal of Intelligent Material Systems and Structures*, vol. 24, no. 3, pp. 334–346, 2013.